Available online at www.sciencedirect.com
SCIENCE DIRECT®
PERGAMON
International Journal of Heat and Mass Transfer 46 (2003) 1827–1840
International Journal of HEAT and MASS TRANSFER
www.elsevier.com/locate/ijhmt

Large eddy simulation of heat and mass transport in turbulent flows. Part 2: Scalar field

Farhad A. Jaberi [a,*], Paul J. Colucci [b]

[a] Department of Mechanical Engineering, Michigan State University, East Lansing, MI 48824-1226, USA
[b] Fluent Inc., Ann Arbor, MI 48104, USA

Received 29 January 2002; received in revised form 7 November 2002

Abstract

Several subgrid-scale (SGS) scalar flux (τ_{iA}) and unmixedness (λ_{AB}) models are presented for large eddy simulation (LES) of heat and mass transport in turbulent flows. The models are similar to those considered in [Int. J. Heat Mass Transfer, in press] for SGS stresses and are based on the information residing at filtered or resolved field. All closures are implemented "locally" and are assessed a priori and a posteriori via data generated by direct numerical simulations of several nonreacting and reacting turbulent flows. A priori assessment indicates that the local values of τ_{iA} and λ_{AB} obtained by new "serial decomposition" closures are closer to "true" values than those obtained by dynamic-diffusivity and two-parameter mixed models. A posteriori assessment also indicates that the statistics of the scalar field in non-reacting and reacting flows are better predicted by LES when new SGS models are used.

1. Introduction

The mathematical model representing heat and mass transport in turbulent flows (reacting or nonreacting) involves several nonlinear and coupled partial differential equations for velocity, scalar and temperature fields. In large eddy simulation (LES) of turbulent mixing and reaction, a spatially filtered form of the velocity and scalar (temperature and species concentration) transport equations are solved together with some closures for residual or subgrid-scale (SGS) fluctuations. The closures are due to subgrid correlations between velocity components (SGS stresses), velocity and scalars (SGS scalar fluxes) and scalars (SGS unmixedness) [2–4]. Jaberi and Colucci [1] discuss the physical nature of the SGS stresses and present several similarity-type closures for modeling of these terms. Here, we extend the models to include the scalar field and discuss the behavior of the SGS scalar in various reacting and nonreacting turbulent flows.

Among various SGS LES models proposed for scalar transport in turbulent flows, the probability density function (PDF), the eddy-diffusivity, and the similarity models have been the most popular ones [2,5–13]. In "assumed PDF" methods, a *Pearson* family of PDFs have been used to model the SGS reactant conversion rate in reacting flows [14]. In "direct PDF" methods, the joint SGS scalar PDFs (termed the filtered density function, FDF) is obtained via numerical solution of its transport equation [13,15]. The latter can be used for both reacting and nonreacting flows and appears to be a very promising methodology for LES of turbulent combustion. In similarity and mixed models, the SGS correlations are evaluated based on the information residing at large or resolved scales. This approach is well justified in nonreacting flows but has some limitations in reacting flows. Despite these limitations, the models constructed based on the resolved field variables remain attractive as they are relatively inexpensive and easy to implement.

The main objectives of this work are to understand the subgrid transport of scalars in turbulent flows and to develop/test closures which are solely based on the resolved field variables. We specifically address the modeling of the SGS scalar flux, τ_{iA} and the SGS

* Corresponding author. Tel.: +1-517-432-4678; fax: +1-517-353-1750.
E-mail address: jaberi@egr.msu.edu (F.A. Jaberi).

0017-9310/03/$ - see front matter © 2003 Elsevier Science Ltd. All rights reserved.
doi:10.1016/S0017-9310(02)00485-4

Nomenclature

A	mass fraction of species $\mathscr{A}$
B	mass fraction of species $\mathscr{B}$
C_{iA}	cross part of SGS scalar flux vector
C_{AB}	cross part of SGS unmixedness
Da	Damkohler number
k	magnitude of the Fourier wavenumber
L_{iA}	Leonard part of SGS scalar flux vector
L_{AB}	Leonard part of SGS unmixedness
p	pressure
P	product mass fraction
Pr	Prandtl number
R_{iA}	Reynolds part of SGS scalar flux vector
R_{AB}	Reynolds part of SGS unmixedness
Re_0	reference Reynolds number
Re_λ	Taylor micro-scale Reynolds number
S	magnitude of rate of strain tensor
Sc	Schmidt Number
$\overline{S}_{ij}$	mean rate of strain tensor
t	time
T_{iA}	residual scalar flux at test-level
u_i	ith component of the fluid velocity vector
x_i	Cartesian coordinates ($x_1 = x$, $x_2 = y$, $x_3 = z$).

Greek symbols

α	ratio of grid-level to test-level filter sizes
δx	grid spacing
$\overline{\Delta}$	characteristic size of the grid-level filter
$\widehat{\overline{\Delta}}$	characteristic size of the test-level filter
ϵ_A	dissipation rate of scalar A
Γ	molecular diffusivity
Γ_t	SGS diffusivity
λ_{AB}	SGS unmixedness
Λ_{AB}	residual unmixedness at test-level
ν_t	SGS viscosity
ρ	correlation coefficient
τ_{ij}	SGS stress tensor
τ_{iA}	SGS scalar flux vector

Superscripts

$\overline{\ }$	grid-level filtering operator
$\widehat{\ }$	test-level filtering operator
$'$	SGS fluctuations

unmixedness, λ_{AB} for constant-density nonreacting and isothermal reacting turbulent flows. For these flows, the SGS stresses are not affected by the reaction and their modeling are not discussed. Several diffusivity and similarity closures are considered and are tested via detailed a priori and a posteriori analysis of the data gathered from DNS and LES of three-dimensional (3D) homogeneous isotropic turbulence, homogeneous shear turbulence, and temporal-developing mixing layers.

2. Mathematical considerations and modeling

For a constant density Newtonian and Fickian fluid, the normalized filtered transport equation of scalar $\mathscr{A}$ (A is the normalized temperature or the mass fraction of a (non)reactive species) in a turbulent flow is given by:

$$\frac{\partial \overline{A}}{\partial t} + \frac{\partial(\overline{u}_i \overline{A})}{\partial x_i} = \frac{1}{Re_0 Pr}\frac{\partial^2 \overline{A}}{\partial x_i \partial x_i} - \frac{\partial \tau_{iA}}{\partial x_i} + \overline{\dot{\omega}}, \tag{1}$$

where u_i is the turbulent velocity in x_i direction, t represents time, and the over-bar denotes the grid-level convolution filter [16]. All variables in the above equation are normalized using reference length, velocity, density and scalar scales. Consequently, the important nondimensional parameters are the Reynolds, Re_0 and the Prandtl number, Pr (or the Schmidt number, Sc). The last term on RHS of Eq. (1) represents the chemical source, or sink term and is zero in nonreacting flows. For a binary isothermal reaction of the type $\mathscr{A} + \mathscr{B} \rightarrow \mathscr{P}$, $\overline{\dot{\omega}}$ is

$$\overline{\dot{\omega}} = -Da\overline{AB} = -Da(\overline{A}\,\overline{B} + \lambda_{AB}), \tag{2}$$

where Da is the Damköhler number, and B is the mass fraction of species $\mathscr{B}$. The transport equation for species $\mathscr{B}$ is similar to that of $\mathscr{A}$ and $Sc = Pr$ for both species.

In Eq. (1), the SGS scalar flux, $\tau_{iA} = \overline{u_i A} - \overline{u}_i\overline{A}$, and the SGS unmixedness, $\lambda_{AB} = \overline{AB} - \overline{A}\,\overline{B}$ require modeling while $\overline{u}_i$ (which not affected by an isothermal reaction) is obtained from the numerical solution of the filtered Navier-Stokes equations as discussed in Ref. [1]. In this paper, we discuss the solution of Eq. (1) and the modeling of SGS scalar flux and unmixedness. The SGS unmixedness, λ_{AB} represents the unclosed part of the filtered reaction rate in a reacting flow or simply the SGS (co)variance in a nonreacting flow.

2.1. Subgrid-scale unmixedness

With "standard" models for SGS flux, dissipation and triple-correlation of λ_{AB}, a closed (modeled) transport equation for λ_{AB} is

$$\begin{aligned}\frac{\partial \lambda_{AB}}{\partial t} + \frac{\partial(\overline{u}_i \lambda_{AB})}{\partial x_i} = {} & \frac{\partial}{\partial x_i}\left[(\Gamma + \Gamma_t)\frac{\partial \lambda_{AB}}{\partial x_i}\right] - C_\epsilon \lambda_{AB} \\ & + 2\Gamma_t\left(\frac{\partial \overline{A}}{\partial x_i}\frac{\partial \overline{B}}{\partial x_i}\right) \\ & + C_{trp} Da\left(\frac{\partial(\overline{A}+\overline{B})}{\partial x_i}\right) \\ & \times \left(\frac{\partial(\overline{A}\,\overline{B})}{\partial x_i} + \frac{\partial \lambda_{AB}}{\partial x_i}\right),\end{aligned} \tag{3}$$

where $\Gamma = 1/Re_0 Pr$, and Γ_t are the molecular and the SGS turbulence diffusivity coefficients, respectively. Eq. (13) reduces to a simple gradient model for λ_{AB} by assuming that the production and dissipation of λ_{AB} are in balance and $\Gamma_t \propto \nu_t$, $C_\epsilon \propto \nu_t/\overline{\Delta}^2$ (ν_t is turbulent viscosity and $\overline{\Delta}$ is the characteristic length scale of the filter function)

$$\lambda_{AB} = C_{U1}\overline{\Delta}^2\left(\frac{\partial\overline{A}}{\partial x_i}\frac{\partial\overline{B}}{\partial x_i}\right). \tag{4}$$

The model labeled UNM1 here. The model coefficient, C_{U1} may be kept constant or may be calculated via dynamic procedure [17]. In the dynamic procedure, a test-scale filtering operator (represented by "hat" and a characteristic filter size of $\widehat{\overline{\Delta}}$) is applied to Eq. (1), yielding an equation for $\widehat{\overline{A}}$ with test-scale scalar flux, $T_{iA} = \widehat{\overline{u_i A}} - \widehat{\overline{u}}_i\widehat{\overline{A}}$, and test-scale unmixedness, $\Lambda_{AB} = \widehat{\overline{AB}} - \widehat{\overline{A}}\widehat{\overline{B}}$ as unknowns. The grid- and the test-level SGS unmixedness are related by the following (Germano) identity

$$\Theta = \widehat{\overline{A}\overline{B}} - \widehat{\overline{A}}\widehat{\overline{B}} = \Lambda_{AB} - \widehat{\lambda_{AB}}, \tag{5}$$

where Θ is the resolved SGS unmixedness. Finally, with a gradient closure for Λ_{AB} (i.e. $\Lambda_{AB} = C_{U1}\widehat{\overline{\Delta}}^2\frac{\partial\widehat{\overline{A}}}{\partial x_i}\frac{\partial\widehat{\overline{B}}}{\partial x_i}$) Eq. (5) yields

$$C_{U1} = \frac{\widehat{\overline{A}\overline{B}} - \widehat{\overline{A}}\widehat{\overline{B}}}{\widehat{\overline{\Delta}}^2\left(\frac{\partial\widehat{\overline{A}}}{\partial x_i}\frac{\partial\widehat{\overline{B}}}{\partial x_i}\right) - \overline{\Delta}^2\left(\widehat{\frac{\partial\overline{A}}{\partial x_i}\frac{\partial\overline{B}}{\partial x_i}}\right)}. \tag{6}$$

This is a "dynamic" expression for model coefficient which is derived based on the assumption that the coefficient does not vary significantly within the test filter domain.

For a filter that convolves in space, there is some information in the SGS unmixedness that can be explicitly calculated. To extract this information, λ_{AB} is decomposed as,

$$\begin{aligned}
&\lambda_{AB} = L_{AB} + C_{AB} + R_{AB}, \\
&L_{AB} = \overline{\overline{A}\overline{B}} - \overline{\overline{A}}\,\overline{\overline{B}}, \\
&C_{AB} = (\overline{\overline{A}B'} - \overline{\overline{A}}\,\overline{B'}) + (\overline{A'\overline{B}} - \overline{A'}\,\overline{\overline{B}}), \\
&R_{AB} = \overline{A'B'} - \overline{A'}\,\overline{B'},
\end{aligned} \tag{7}$$

where for any variable f, $f' = f - \overline{f}$. The terms L_{AB}, C_{AB} and R_{AB} has the same properties as λ_{AB} and are referred to as the (generalized) Leonard, the (generalized) cross and the (generalized) Reynolds terms, respectively. The Leonard term is closed and needs no modeling.

Similarly, Λ_{AB} is decomposed as:

$$\Lambda_{AB} = L^T_{AB} + C^T_{AB} + R^T_{AB}, \tag{8}$$

where

$$\begin{aligned}
&L^T_{AB} = \widehat{\overline{\overline{A}\overline{B}}} - \widehat{\overline{\overline{A}}}\,\widehat{\overline{\overline{B}}}, \\
&C^T_{AB} = (\widehat{\overline{\overline{A}B'}} - \widehat{\overline{\overline{A}}}\,\widehat{\overline{B'}}) + (\widehat{\overline{A'\overline{B}}} - \widehat{\overline{A'}}\,\widehat{\overline{\overline{B}}}), \\
&R^T_{AB} = \widehat{\overline{A'B'}} - \widehat{\overline{A'}}\,\widehat{\overline{B'}}.
\end{aligned} \tag{9}$$

Following a procedure similar to that used by Salvetti and Banerjee [8], a two-parameter mixed model is constructed for λ_{AB},

$$\lambda_{AB} = C_{U2a}L_{AB} + C_{U2b}\overline{\Delta}^2\left(\frac{\partial\overline{A}}{\partial x_i}\frac{\partial\overline{B}}{\partial x_i}\right). \tag{10}$$

Here, we assume that C_{AB} is proportional to L_{AB} and R_{AB} and is modeled with a diffusivity closure similar to that in Eq. (4). The traditional dynamic approach (outlined above) cannot be used to calculate the model coefficients because there are two unknowns (C_{U2a} and C_{U2b}) and only one equation (Eq. (5)). Here, we assume "scale similarity" between C_{AB} and C^T_{AB} and between R_{AB} and R^T_{AB} to calculate the model coefficients as

$$\begin{aligned}
C_{U2a} &= \frac{(\widehat{\overline{\overline{A}\overline{B'}}} - \widehat{\overline{\overline{A}}}\,\widehat{\overline{\overline{B'}}}) + (\widehat{\overline{A'\overline{B}}} - \widehat{\overline{A'}}\,\widehat{\overline{\overline{B}}})}{\widehat{\overline{\overline{A}}}\,\widehat{\overline{\overline{B}}} - \widehat{\overline{\overline{A}}}\,\widehat{\overline{\overline{B}}}}, \\
C_{U2b} &= \frac{\widehat{\overline{A'B'}} - \widehat{\overline{A'}}\,\widehat{\overline{B'}}}{\widehat{\overline{\Delta}}^2\left(\frac{\partial\widehat{\overline{A}}}{\partial x_i}\frac{\partial\widehat{\overline{B}}}{\partial x_i}\right) - \overline{\Delta}^2\left(\widehat{\frac{\partial\overline{A}}{\partial x_i}\frac{\partial\overline{B}}{\partial x_i}}\right)}.
\end{aligned} \tag{11}$$

Eqs. (10) and (11) represent a dynamic mixed closure, termed UNM2. The assumption that C_{AB} and R_{AB} are proportional to L_{AB} yields a similarity model for λ_{AB},

$$\lambda_{AB} = C_{U3}L_{AB} = C_{U3}(\overline{\overline{A}\overline{B}} - \overline{\overline{A}}\,\overline{\overline{B}}), \quad C_{U3} = \frac{\widehat{\overline{\overline{A}\overline{B}}} - \widehat{\overline{\overline{A}}}\,\widehat{\overline{\overline{B}}}}{\widehat{\overline{\overline{A}}}\,\widehat{\overline{\overline{B}}} - \widehat{\overline{\overline{A}}}\,\widehat{\overline{\overline{B}}}}, \tag{12}$$

which is similar to those proposed in Refs. [18,19] and is labeled as UNM3 here.

For a filter allowing overlap between residual and filtered fields, part of C_{AB} and R_{AB} may be calculated by decomposing them into the Leonard, the cross and the Reynolds terms of their own,

$$\begin{aligned}
C_{AB} = &\underbrace{(\overline{\overline{\overline{A}}\,\overline{B'}} - \overline{\overline{\overline{A}}}\,\overline{\overline{B'}}) + (\overline{\overline{A'}\,\overline{\overline{B}}} - \overline{\overline{A'}}\,\overline{\overline{\overline{B}}})}_{\text{(I)}} \\
&+ \underbrace{(\overline{\overline{\overline{A}}(B')'} - \overline{\overline{\overline{A}}}\,\overline{(B')'}) + (\overline{(A')'\overline{\overline{B}}} - \overline{(A')'}\,\overline{\overline{\overline{B}}})}_{\text{(II)}} \\
&+ \underbrace{2(\overline{\overline{A'}\,\overline{B'}} - \overline{\overline{A'}}\,\overline{\overline{B'}})}_{\text{(III)}} \\
&+ \underbrace{(\overline{\overline{A'}(B')'} - \overline{\overline{A'}}\,\overline{(B')'}) + (\overline{(A')'\overline{B'}} - \overline{(A')'}\,\overline{\overline{B'}})}_{\text{(IV)}},
\end{aligned} \tag{13}$$

$$R_{AB} = \underbrace{(\overline{\overline{A'}\,\overline{B'}} - \overline{\overline{A'}}\,\overline{\overline{B'}})}_{\text{(V)}} + \underbrace{(\overline{\overline{A'}(B')'} - \overline{\overline{A'}}\,\overline{(B')'}) + (\overline{(A')'\overline{B'}} - \overline{(A')'}\,\overline{\overline{B'}})}_{\text{(VI)}} + \underbrace{(\overline{(A')'(B')'} - \overline{(A')'}\,\overline{(B')'})}_{\text{(VII)}}, \quad (14)$$

where, $(A')' = A' - \overline{A'} = A - 2\overline{A} + \overline{\overline{A}}$ and $(B')' = B' - \overline{B'} = B - 2\overline{B} + \overline{\overline{B}}$. Terms (I), (III), and (V) are closed but the remaining terms are not. An interesting observation is that the Leonard and the cross parts of R_{AB} (i.e. terms (V) and (VI)) are the same as terms (III) and (IV). This suggests that C_{AB} and R_{AB} are at least moderately correlated.

Substituting Eqs. (13) and (14) into Eq. (7) yields

$$\lambda_{AB} = \phi_{AB} + \psi_{AB}, \quad (15)$$

where,

$$\phi_{AB} = (\overline{\overline{A}\,\overline{B}} - \overline{\overline{A}}\,\overline{\overline{B}}) + (\overline{\overline{\overline{A}}\,\overline{B'}} - \overline{\overline{\overline{A}}}\,\overline{\overline{B'}} + \overline{\overline{A'}\,\overline{\overline{B}}} - \overline{\overline{A'}}\,\overline{\overline{B}}) + 3(\overline{\overline{A'}\,\overline{B'}} - \overline{\overline{A'}}\,\overline{\overline{B'}}),$$

and

$$\psi_{AB} = (\overline{x_A y_B} - \overline{x}_A \overline{y}_B) + (\overline{y_A x_B} - \overline{y}_A \overline{x}_B),$$
$$x_A = \tfrac{1}{2}(A + 2\overline{A} - \overline{\overline{A}}), \quad x_B = \tfrac{1}{2}(B + 2\overline{B} - \overline{\overline{B}}),$$
$$y_A = A - 2\overline{A} + \overline{\overline{A}}, \quad y_B = B - 2\overline{B} + \overline{\overline{B}},$$

are the "known" and "unknown" parts of the SGS unmixedness, respectively.

By neglecting the cross and the Reynolds parts of ψ_{AB},

$$\psi_{AB} = \overline{\overline{x}_A \overline{y}_B} - \overline{\overline{x}}_A \overline{\overline{y}}_B + \overline{\overline{y}_A \overline{x}_B} - \overline{\overline{y}}_A \overline{\overline{x}}_B. \quad (16)$$

Eqs. (15) and (16) represent a new serial decomposition closure for λ_{AB}, termed UNM4. By assuming that the cross and the Reynolds parts of ψ_{AB} are proportional to its Leonard part,

$$\psi_{AB} = C_{U5}(\overline{\overline{x}_A \overline{y}_B} - \overline{\overline{x}}_A \overline{\overline{y}}_B + \overline{\overline{y}_A \overline{x}_B} - \overline{\overline{y}}_A \overline{\overline{x}}_B), \quad (17)$$

and we obtain another serial decomposition model for λ (termed UNM5) here. The model coefficient, C_{U5} is dynamically calculated as:

$$C_{U5} = \frac{(\widehat{\overline{x}_A \overline{y}_B} - \widehat{\overline{x}}_A \widehat{\overline{y}}_B) + (\widehat{\overline{y}_A \overline{x}_B} - \widehat{\overline{y}}_A \widehat{\overline{x}}_B)}{(\widehat{\overline{\overline{x}}_A \overline{\overline{y}}_B} - \widehat{\overline{\overline{x}}}_A \widehat{\overline{\overline{y}}}_B) + (\widehat{\overline{\overline{y}}_A \overline{\overline{x}}_B} - \widehat{\overline{\overline{y}}}_A \widehat{\overline{\overline{x}}}_B)}. \quad (18)$$

The moderate correlation between C_{AB} and the Leonard part of R_{AB} ($\Re_{AB}$), as indicated in Eqs. (13) and (14), also suggests the following closure (termed UNM6) for the SGS unmixedness:

$$\lambda_{AB} = (\overline{\overline{A}\,\overline{B}} - \overline{\overline{A}}\,\overline{\overline{B}}) + C_{U6}(\overline{\overline{A'}\,\overline{B'}} - \overline{\overline{A'}}\,\overline{\overline{B'}}),$$
$$C_{U6} = \frac{(\widehat{\overline{A}\,\overline{B}} - \widehat{\overline{A}}\,\widehat{\overline{B}}) - (\widehat{\overline{\overline{A}}\,\overline{\overline{B}}} - \widehat{\overline{\overline{A}}}\,\widehat{\overline{\overline{B}}})}{(\widehat{\overline{A'}\,\overline{B'}} - \widehat{\overline{A'}}\,\widehat{\overline{B'}})}. \quad (19)$$

A modified version of this model may be used for a sharp cut off filter function in Fourier space. For this filter, $\overline{A'}$ and $\overline{B'}$ in Eq. (19) are replaced by $\overline{A''} = \overline{A} - \widehat{\overline{A}}$ and $\overline{B''} = \overline{B} - \widehat{\overline{B}}$. Results of our a priori analysis, as obtained by the box filter, indicates that the original and modified versions of UNM6 have the same accuracy.

2.2. Subgrid-scale scalar flux

In this section, we present several SGS scalar flux closures which are similar to SGS unmixedness models in Section 2.1 (all models are listed in Table 1). The most popular closure for τ_{iA} is the eddy diffusivity closure [5]

$$\tau_{iA} = -C_{S1}\overline{\Delta}^2 |\overline{S}| \frac{\partial \overline{A}}{\partial x_i}, \quad (20)$$

where C_{S1} is the model coefficient, and $|\overline{S}| = (2\overline{S}_{ij}\overline{S}_{ij})^{1/2}$, $\overline{S}_{ij} = \frac{1}{2}(\frac{\partial \overline{u}_i}{\partial x_j} + \frac{\partial \overline{u}_j}{\partial x_i})$, is the norm of the strain rate tensor. In the dynamic version of this model (termed SFM1 here), C_{S1} is calculated locally and dynamically by using a similar diffusivity closure for the test-level scalar flux (T_{iA}) [6,7].

For development of similarity and mixed closures, τ_{iA} is decomposed as:

$$\tau_{iA} = L_{iA} + C_{iA} + R_{iA}, \quad (21)$$

Table 1
A list of SGS scalar flux and unmixedness closures

Model #	Model type	SGS scalar flux model	SGS unmixedness model
1	Diffusivity	SFM1, Eq. (20)	UNM1, Eq. (4)
2	Mixed	SFM2, Eq. (22)	UNM2, Eq. (10)
3	Similarity	SFM3, Eq. (23)	UNM3, Eq. (12)
4	Serial decomposition 1	SFM4, Eqs. (26) and (27)	UNM4, Eqs. (15) and (16)
5	Serial decomposition 2	SFM5, Eqs. (26) and (28)	UNM5, Eqs. (15) and (17)
6	Serial decomposition 3	SFM6, Eq. (29)	UNM6, Eq. (19)

where,

$$L_{iA} = \overline{\overline{u}_i\overline{A}} - \overline{\overline{u}}_i\overline{\overline{A}},$$
$$C_{iA} = (\overline{\overline{u}_iA'} - \overline{\overline{u}}_i\overline{A'}) + (\overline{u_i'\overline{A}} - \overline{u_i'}\overline{\overline{A}}),$$
$$R_{iA} = \overline{u_i'A'} - \overline{u_i'}\,\overline{A'},$$

are the Leonard, the cross and the Reynolds parts of τ_{iA}, respectively. T_{iA} is similarly decomposed to its Leonard (L_{iA}^T), cross (C_{iA}^T) and Reynolds (R_{iA}^T) parts.

In the dynamic two-parameter mixed model of [8] (referred to as SFM2 here), C_{iA} is assumed to be proportional to L_{iA}, and R_{iA} is modeled by a diffusivity closure. With these approximations,

$$\tau_{iA} = -C_{\mathrm{S2a}}\overline{\Delta}^2|\overline{S}|\frac{\partial\overline{A}}{\partial x_i} + C_{\mathrm{S2b}}L_{iA}, \tag{22}$$

where the model coefficients C_{S2a} and C_{S2b} are calculated dynamically.

Alternatively, we may assume C_{iA} and R_{iA} are proportional to L_{iA}, and develop the following similarity model for τ_{iA}:

$$\tau_{iA} = C_{\mathrm{S3}}L_{iA} = C_{\mathrm{S3}}(\overline{\overline{u}_i\overline{A}} - \overline{\overline{u}}_i\overline{\overline{A}}), \tag{23}$$
$$C_{\mathrm{S3}} = \frac{G_{iA}H_{iA}}{H_{iA}H_{iA}},$$
$$G_{iA} = \widehat{\overline{u}_i\overline{A}} - \widehat{\overline{u}}_i\widehat{\overline{A}} = T_{iA} - \widehat{\tau_{iA}},$$
$$H_{iA} = \widehat{\overline{\overline{u}}_i\overline{\overline{A}}} - \widehat{\overline{\overline{u}}}_i\widehat{\overline{\overline{A}}}.$$

This model is referred to as SFM3.

The idea of serial decomposition, as outlined in Section 2.1, is the basis of several new models for τ_{iA}. First, the Leonard and the cross parts of τ_{iA} are decomposed as:

$$\begin{aligned} C_{iA} = {} & \underbrace{(\overline{\overline{\overline{u}}_i\overline{A'}} - \overline{\overline{\overline{u}}}_i\overline{\overline{A'}}) + (\overline{\overline{u_i'}\overline{A}} - \overline{\overline{u'}}_i\overline{\overline{A}})}_{\text{(I)}} \\ & + \underbrace{(\overline{\overline{\overline{u}}_i(A')'} - \overline{\overline{\overline{u}}}_i\overline{(A')'}) + (\overline{(u')_i'\overline{A}} - \overline{(u')'}_i\overline{\overline{A}})}_{\text{(II)}} \\ & + \underbrace{2(\overline{\overline{u}_i'\overline{A'}} - \overline{\overline{u'}}_i\overline{\overline{A'}})}_{\text{(III)}} \\ & + \underbrace{(\overline{\overline{u}_i'(A')'} - \overline{\overline{u'}}_i\overline{(A')'}) + (\overline{(u')_i'\overline{A'}} - \overline{(u')'}_i\overline{\overline{A'}})}_{\text{(IV)}}, \end{aligned} \tag{24}$$

$$\begin{aligned} R_{iA} = {} & \underbrace{(\overline{\overline{u}_i'\overline{A'}} - \overline{\overline{u'}}_i\overline{\overline{A'}})}_{\text{(V)}} \\ & + \underbrace{(\overline{\overline{u}_i'(A')'} - \overline{\overline{u'}}_i\overline{(A')'}) + (\overline{(u')_i'\overline{A'}} - \overline{(u')'}_i\overline{\overline{A'}})}_{\text{(VI)}} \\ & + \underbrace{(\overline{(u')_i'(A')'} - \overline{(u')'}_i\overline{(A')'})}_{\text{(VII)}}, \end{aligned} \tag{25}$$

with, $(u_i')' = u_i' - \overline{u_i'} = u_i - 2\overline{u_i} + \overline{\overline{u_i}}$. Then, Eqs. (21), (24) and (25) are written as

$$\tau_{iA} = \phi_{iA} + \psi_{iA}, \tag{26}$$

where,

$$\begin{aligned} \phi_{iA} = {} & (\overline{\overline{u}_i\overline{A}} - \overline{\overline{u}}_i\overline{\overline{A}}) + (\overline{\overline{\overline{u}}_i\overline{A'}} - \overline{\overline{\overline{u}}}_i\overline{\overline{A'}} + \overline{\overline{u_i'}\overline{\overline{A}}} - \overline{\overline{u'}}_i\overline{\overline{A}}) \\ & + 3(\overline{\overline{u_i'}\overline{A'}} - \overline{\overline{u'}}_i\overline{\overline{A'}}) \end{aligned}$$

and

$$\psi_{iA} = (\overline{w_i\bar{y}_A} - \overline{w}_i\bar{y}_A) + (\overline{v_i\bar{x}_A} - \overline{v}_i\bar{x}_A),$$
$$w_i = \tfrac{1}{2}(u_i + 2\overline{u}_i - \overline{\overline{u}}_i), \quad v_i = u_i - 2\overline{u}_i + \overline{\overline{u}}_i$$

are the known and unknown parts of τ_{iA}, respectively.

Two new serial decomposition models are proposed for τ_{iA}. In the first one (termed SFM4),

$$\psi_{iA} = \overline{\overline{w}_i\overline{\bar{y}}}_A - \overline{\overline{w}}_i\overline{\overline{\bar{y}}}_A + \overline{\overline{v}_i\overline{\bar{x}}}_A - \overline{\overline{v}}_i\overline{\overline{\bar{x}}}_A, \tag{27}$$

and in the second one (termed SFM5)

$$\psi_{iA} = C_{\mathrm{S5}}(\overline{\overline{w}_i\overline{\bar{y}}}_A - \overline{\overline{w}}_i\overline{\overline{\bar{y}}}_A + \overline{\overline{v}_i\overline{\bar{x}}}_A - \overline{\overline{v}}_i\overline{\overline{\bar{x}}}_A), \tag{28}$$

where C_{S5} is calculated locally using the dynamic procedure.

According to Eqs. (24) and (25), the Leonard part of R_{iA} and C_{iA} are partially correlated. This suggests the following dynamic model (called SFM6) for τ_{iA};

$$\tau_{iA} = (\overline{\overline{u}_i\overline{A}} - \overline{\overline{u}}_i\overline{\overline{A}}) + C_{\mathrm{S6}}(\overline{\overline{V}_i\bar{a}} - \overline{\overline{V}}_i\bar{a}),$$
$$C_{\mathrm{S6}} = \frac{E_{iA}D_{iA}}{D_{iA}D_{iA}}, \tag{29}$$

where,

$$E_{iA} = (\widehat{\overline{u}_i\overline{A}} - \widehat{\overline{u}}_i\widehat{\overline{A}}) - (\widehat{\overline{\overline{u}}_i\overline{\overline{A}}} - \widehat{\overline{\overline{u}}}_i\widehat{\overline{\overline{A}}}), \quad D_{iA} = (\widehat{\overline{\overline{V}}_i\bar{a}} - \widehat{\overline{\overline{V}}}_i\widehat{\bar{a}}).$$

For a sharp cut off filter in Fourier space, a modified version of SFM6 is used. We also tested variety of different dynamic one-, two-, and three-parameter mixed models. Our a priori analysis indicates that none of the tested models are superior to SFM6.

3. Simulations

Direct and LESs of (1) homogeneous isotropic (HI), (2) homogeneous shear (HS), and (3) temporally developing shear layer (TSL) of both nonreacting and reacting turbulent flows are conducted. The shear layers are simulated with no initial 3D perturbations in TSL1 and with added initial random solenoidal 3D velocity fluctuations in TSL2. The numerical procedure in both DNS and LES is similar to that used in our previous works [20–24]. The spatial discretization is via a spectral-collocation numerical scheme utilizing Fourier basis functions and time advancement is via second order

Adams–Bashforth method. The boundary conditions and initial velocity field are similar to those in Ref. [1]. Some of the specifications of four DNS cases that are considered in this study are listed in Table 2 of Ref. [1]. In HI and HS flows, the initial scalar fields are specified in the physical domain as square waves (slabs) with scalar $\mathscr{B}$ perfectly anti-correlated with $\mathscr{A}$ [20]. The scalars have no mean gradient; hence their *rms* fluctuations decay in time [20]. In TSL flows, the scalars, $\mathscr{A}$ and $\mathscr{B}$, are introduced into the high- and low-speed streams, respectively. The molecular Schmidt number is 0.7 in all simulations.

Both the "exact" and the "approximate" versions of box filter in physical space are used in LES. This filter function does not violate the realizability condition for scalar field and yields results qualitatively similar to those obtained with a Gaussian filter. The exact version is used for calculating the true SGS quantities by averaging over fine (DNS) grid points. The filter size at grid-level ($\overline{\Delta}$) is set to be twice of the grid spacing in LES ($(\delta x)_{\mathrm{LES}}$) and the filter size at test-level ($\widehat{\Delta}$) is twice of that at grid-level (i.e. $\alpha = 2$).

The resolution in DNS is dictated by the magnitudes of the physical parameters, with sufficient testing on the independency of the results to the grid resolution. Simulations of HI and HS flows are conducted within a cubic box containing 128^3 collocation points. The resolution for DNS of TSL flows is 96^3. The resolution in LES is specified by the ratio of the filter size at grid-level to the grid spacing in DNS ($\mathscr{R} = \overline{\Delta}/(\delta x)_{\mathrm{DNS}}$). For example, with 128^3 collocation points in DNS and $\mathscr{R} = 8$, the resolution in LES would be 32^3. Four different approximate box filters are considered (Table 2). In the first one (FILT#1), the filtered values are evaluated by trapezoidal rule [25,26] and $\mathscr{R} = 8$. The second (FILT#2) and the third (FILT#3) filter functions are similar to FILT#1 but with $\mathscr{R} = 12$ and 16, respectively. In the fourth filter function (FILT#4), the size of filter is the same as that in FILT#1 but the filtered variables are calculated by averaging with equal weight for all grid values. In all simulations (both DNS and LES), the grid spacing in all directions are uniform and equal.

The comparison between DNS and LES is made a priori and a posteriori. In a priori analysis, the subgrid quantities as calculated directly from DNS data are compared. In a posteriori analysis, the statistics of the resolved variables as predicted by LES are compared with those obtained from the DNS data. The models are tested in a localized manner without any averaging over homogeneous directions. For HI and HS flows, the temporal evolution of the volumetric averaged statistics are of primary importance and are presented. For TSL flows the averaging are conducted over x–y planes (represented by $[\ ]$) and the y-dependent statistics are considered. In some cases the volumetric averaged statistics for TSL flows are also reported. Of primary statistical quantities that are considered below are the correlation coefficient between variables α_1 and α_2, denoted by $\zeta(\alpha_1, \alpha_2)$ and the PDFs of subgrid and resolved variables.

Table 2
The filter functions

Filter	$\overline{\Delta}/(\delta x)_{\mathrm{DNS}}$	Filter approximation
FILT#1	8	Trapezoidal
FILT#2	12	Trapezoidal
FILT#3	16	Trapezoidal
FILT#4	8	Equal-weighting

4. Results of a priori analysis

The results of our a priori analysis are presented in two different sections in which the modeling of the SGS scalar flux and the SGS unmixedness are discussed separately.

4.1. Subgrid-scale scalar flux

The decomposition of SGS scalar flux into the Leonard, the cross and the Reynolds terms, as argued in Section 2.2 will result in less modeling and improved evaluation of τ_{iA} since L_{iA} may be explicitly calculated and C_{iA} and R_{iA} may be separately modeled.

Several different diffusivity and similarity base closures for the Leonard, the cross and the Reynolds parts of τ_{iA}, are evaluated in Table 3, where the time-averaged values of the correlation coefficients between C_{1A}/R_{1A} and $L_{iA}/\overline{\Delta}^2|\overline{S}|\frac{\partial\overline{A}}{\partial x_i}/\mathfrak{R}_{iA}\mathfrak{R}_{iA}$ are listed. The results in this table indicate that the local values of C_{1A} and R_{1A} are poorly predicted by the gradient models. In contrast, the similarity closures are reasonably accurate. Our results (not shown) also indicate that the contributions of L_{1A} and C_{1A} are comparable to R_{1A} and fairly independent of the (rate of) reaction in all flows and at all times. All of these suggest that the similarly type models are potentially the most accurate.

The SGS scalar flux models discussed in Section 2.2 and listed in Table 1 (i.e. SFM1 to SFM6), are assessed

Table 3
The time averaged correlation coefficients in different flows

Correlation coefficient	HI	HS
$\zeta(C_{iA}, L_{iA})$	0.702	0.689
$\zeta(C_{iA}, -\overline{\Delta}^2\|\overline{S}\|\frac{\partial\overline{A}}{\partial x_i})$	0.332	0.250
$\zeta(C_{iA}, \mathfrak{R}_{iA})$	0.848	0.837
$\zeta(R_{iA}, L_{iA})$	0.361	0.349
$\zeta(R_{iA}, -\overline{\Delta}^2\|\overline{S}\|\frac{\partial\overline{A}}{\partial x_i})$	0.304	0.249
$\zeta(R_{iA}, \mathfrak{R}_{iA})$	0.635	0.615

in Figs. 1 and 2, where the correlation coefficients and the PDFs of τ_{iA} for HI, HS and TSL1 flows are shown. The "time" t^* in Fig. 1 is the time normalized by the final time of simulation in each case. This time is adopted to make comparison between various flows more convenient. Fig. 1 shows that the local values of τ_{iA}, as calculated by SFM1, correlate rather poorly with those of DNS in all flows.

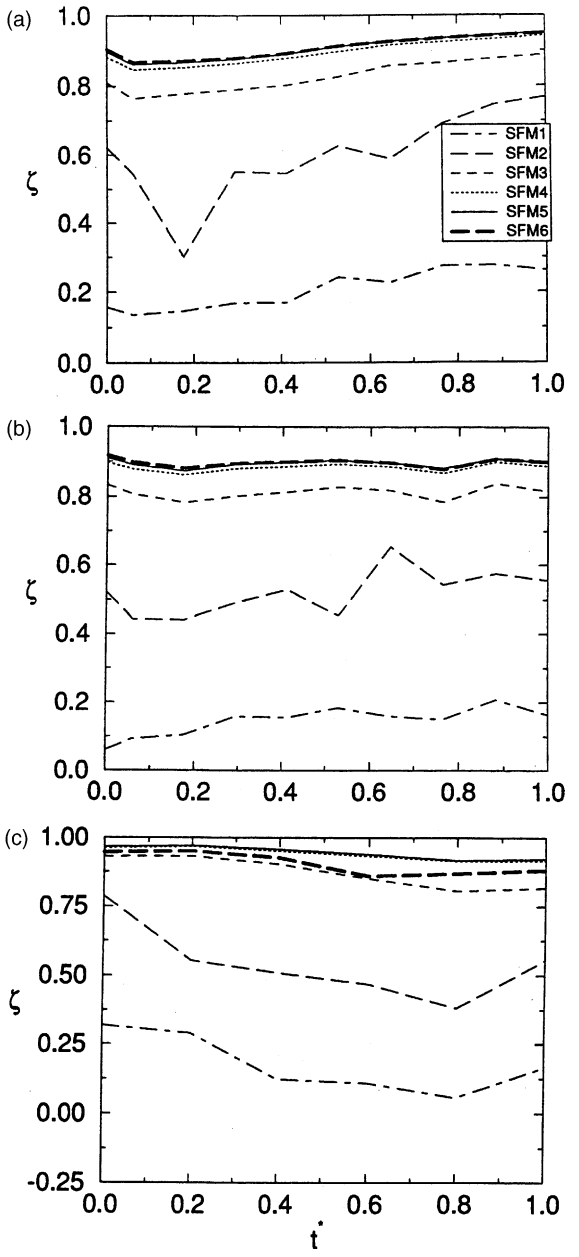

Fig. 1. Temporal variations of the correlation coefficient between the DNS and modeled values of the SGS scalar fluxes in nonreacting flows: (a) HI, (b) HS, and (c) TSL1.

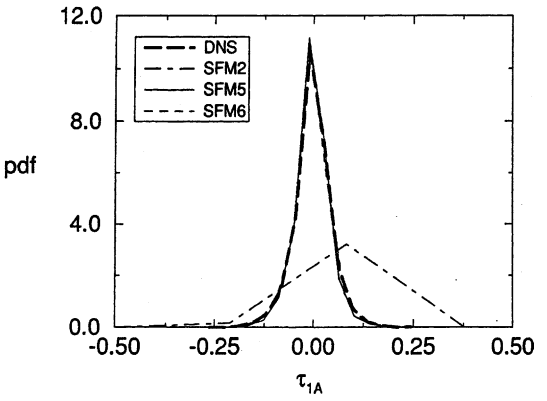

Fig. 2. The PDFs of the SGS scalar flux (τ_{1A}) in HI flow and for $Da = 4$ at $t^* = 0.063$.

The results in Fig. 1 are consistent with those in Table 3 and indicate that the performance of the gradient model is not improved by dynamic evaluation of its coefficient. The accuracy of SFM2 is better than SFM1 but still much less than those of the proposed similarity closures (SFM3 to SFM6). Among the similarity closures, SFM5 and SFM6 are the most accurate and the accuracy of SFM3 is between that of SFM2 and SFM5. The PDFs of τ_{1A} as obtained by the serial decomposition models (SFM5 and SFM6) are also shown in Fig. 2 to be very close to the "true" PDFs; again indicating the accuracy of the serial decomposition closures. The predicted PDF by SFM2 is very different than the true PDF.

To assess the sensitivity of the models to the filter parameters and to the reaction rate, the time averaged values of the correlation coefficients between DNS and modeled SGS scalar fluxes for different filters and Damköhler numbers are considered in Table 4. The tested models exhibit no significant dependency to the rate of reaction. However, the magnitude of the correlation coefficients decrease as the size of the filter increases or the error in the filtering operation increases (i.e. FILT#4 is used). The effects of filtering approximation and filter size on SFM5 and SFM6 are much less than those on SFM2. The results for HI and TSL flows exhibit similar trends to those for HS flow in Table 4.

Table 4
The time averaged correlation coefficient between DNS and modeled values of τ_{iA} for HS flow

Filter type	*Da*	SFM2	SFM5	SFM6
FILT#1	4	0.521	0.895	0.896
FILT#3	4	0.287	0.757	0.760
FILT#4	4	0.386	0.872	0.875
FILT#1	∞	0.520	0.890	0.889

4.2. Subgrid-scale unmixedness

The importance of SGS unmixedness in various reacting flows is demonstrated in Fig. 3(a), where the temporal variation of $\langle \lambda_{AB}/\overline{AB} \rangle$ for HI and HS flows is considered. The results for HI and HS flows are similar and show that the SGS unmixedness becomes more important as the rate of reaction increases. It is also shown in Fig. 3(a) that the average contribution of λ_{AB} decreases in time as mixing/reaction proceeds, leading to a relatively low average values for $|\lambda_{AB}/\overline{AB}|$ at long times. However, Fig. 3(b) shows that the PDF of $\lambda_{AB}/\overline{AB}$ becomes highly skewed (toward -1) as flow evolves, suggesting that even at long times the filtered reaction rate is significantly affected by the SGS scalar correlations at some locations. The SGS unmixedness is always negative and decreases the rate of reaction as expected. This is not to say that SGS fluctuations prevent reaction from occurring; but that the reaction does not proceed at the rate based on the filtered value of the concentrations.

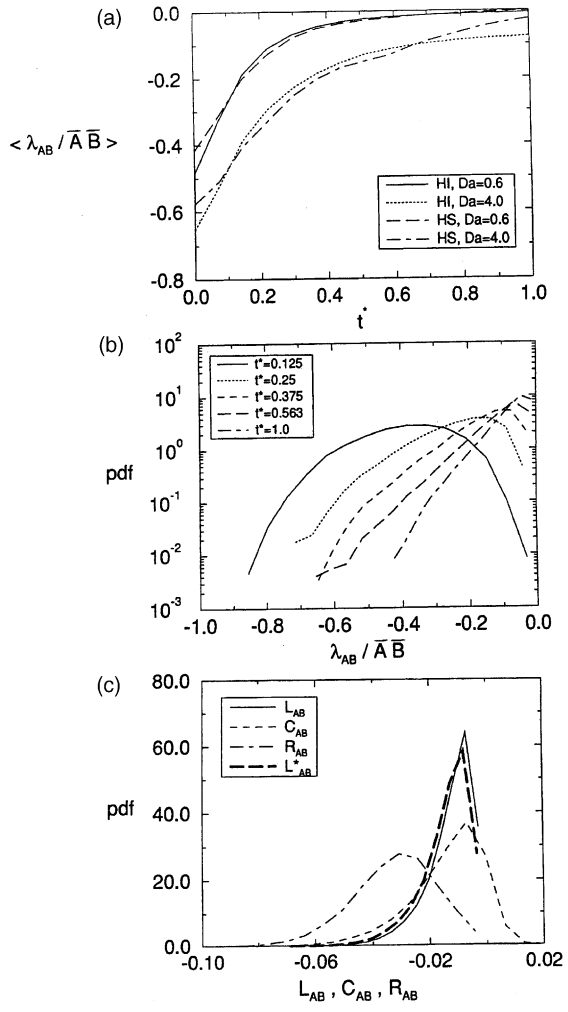

Fig. 3. (a) Temporal variations of the volumetric-averaged normalized SGS unmixedness in HI and HS flows, (b) PDFs of the normalized SGS unmixedness in HI flow for $Da = 4$, (c) the PDFs of the Leonard, the cross and the Reynolds parts of the SGS unmixedness in HI flow for $Da = 0.6$ at $t^* = 0.0625$.

Several of the closures developed in Section 2.1 for λ_{AB} are derived based on the argument that the Leonard, the cross and the Reynolds parts of λ_{AB} (i.e. L_{AB}, C_{AB} and R_{AB}) behave differently but they are all important and should be considered in the modeling of λ_{AB}. This argument is supported by the results presented in Fig. 3(c) for HI flow (the trends are similar in HS and TSL flows). The results in this figure show that the PDFs of L_{AB}, C_{AB} and R_{AB} are indeed very different. While L_{AB} and R_{AB} are mostly negative, C_{AB} attains both positive and negative values. Also, the PDF of R_{AB} is significantly shifted toward the high negative values as compared to the PDFs of L_{AB} and C_{AB}. This is expected since the nonlocal interactions between the subgrid and the resolved scales mainly appear in the Reynolds part of the SGS unmixedness. Also shown in Fig. 3(c) is the PDF of L^*_{AB} as calculated from DNS data over coarse (LES) grids. L_{AB} is obtained via averaging over fine (DNS) grids. In LES, only the information over coarse grids is available; hence it is important to know how L^*_{AB} approximates L_{AB}. Fig. 3(c) shows that the PDFs of L^*_{AB} and L_{AB} are very close, confirming that the Leonard term is accurately calculated over LES grids. Our results (not shown) also indicate that the contributions of L_{AB} and C_{AB}, R_{AB} are comparable and important in all flows regardless of the rate of reaction.

Various base closures for C_{AB} and R_{AB} are tested in Table 5, where the time-averaged correlation coefficients of C_{AB} and R_{AB} with L_{AB}, $\overline{\Delta}^2 \frac{\partial \overline{A}}{\partial x_i} \frac{\partial \overline{B}}{\partial x_i}$ and $\Re_{AB}$ are compared. Evidently, all the tested closures are able to predict the local values of C_{AB} with moderate accuracy. However, the predictions are not as good for R_{AB}. Among different closures, $\Re_{AB}$ exhibits the highest correlation with the local values of C_{AB} and R_{AB}.

The results in Table 5 suggest some moderate accuracy for the gradient Λ_{AB} model. However, the results of our a priori analysis (not shown) indicate that the predictions of the dynamic gradient model (UNM1) are indeed very inaccurate. For example, we have found that

Table 5
The time averaged correlation coefficients in HS flow

Correlation coefficient	$Da = 0.6$	$Da = 4$
$\zeta(C_{AB}, L_{AB})$	0.731	0.726
$\zeta(C_{AB}, \overline{\Delta}^2 \frac{\partial \overline{A}}{\partial x_i} \frac{\partial \overline{B}}{\partial x_i})$	0.770	0.762
$\zeta(C_{AB}, \Re_{AB})$	0.826	0.825
$\zeta(R_{AB}, L_{AB})$	0.492	0.461
$\zeta(R_{AB}, \overline{\Delta}^2 \frac{\partial \overline{A}}{\partial x_i} \frac{\partial \overline{B}}{\partial x_i})$	0.474	0.447
$\zeta(R_{AB}, \Re_{AB})$	0.668	0.603

Table 6
The time averaged correlation coefficients

Correlation coefficients	HI	HS	TSL2[a]
$\zeta(C_t^G, C_g^G)$	0.033	0.017	0.000
$\zeta(C_t^S, C_g^S)$	0.923	0.922	0.971

[a] In HI and HS flows $Da = 4$ and in TSL flow $Da = 1$.

the correlation coefficients between DNS and UNM1 values of λ_{AB} are always less than 0.05 in all flows and at all Damköhler numbers. To explain this behavior, in Table 6 the time averaged values of the correlation coefficients between $C_g^S = L_{AB}^T/T_{AB}$ and $C_t^S = \widehat{L_{AB}}/\widehat{\lambda_{AB}}$ and those between $C_g^G = \widehat{\overline{A}}^2 \frac{\partial \widehat{\overline{A}}}{\partial x_i}\frac{\partial \widehat{\overline{B}}}{\partial x_i}/T_{AB}$ and $C_t^G = \overline{A}^2 \widehat{\frac{\partial \overline{A}}{\partial x_i}\frac{\partial \overline{B}}{\partial x_i}}/\widehat{\lambda_{AB}}$ are considered. C_g^S, C_t^S, C_g^G, C_t^G represent the similarity and the gradient model coefficients at grid- and test-levels. In the derivation of UNM1 and UNM2 it is assumed that there is a strong correlation between the grid- and the test-level coefficients. The results in Table 6 indicate that there is basically no correlation between these coefficients. This explains the poor performance of UNM1 and UNM2. In contrast, the grid- and test-level coefficients of the similarity models (C_g^G, C_t^G) are well correlated which explains the better performance of the dynamic similarity closures.

Temporal evolution of the correlation coefficients between the modeled and the true (DNS) values of λ_{AB} in HI, HS and TSL flows are shown in Fig. 4. The results in this figure demonstrate the ability of UNM3, UNM4, UNM5 and UNM6 to accurately predict the local values of λ_{AB}. Despite some variations in time, the correlations coefficients as obtained with these models remain fairly high throughout the simulations in all flows. Evidently, UNM4, UNM5 and UNM6 are more accurate than UNM3. The proposed serial-decomposition closures are able to predict the local values of the test-level SGS unmixedness, Λ_{AB}, even better than the grid-level unmixedness, λ_{AB}. The nonlocal interactions between the subgrid and the resolved field quantities are less important at test-level; therefore, the test-level unmixedness is better predicted. Our results (not shown) also indicate that the PDF of λ_{AB} is also reasonably well predicted by the serial decomposition models in all flows and at all times.

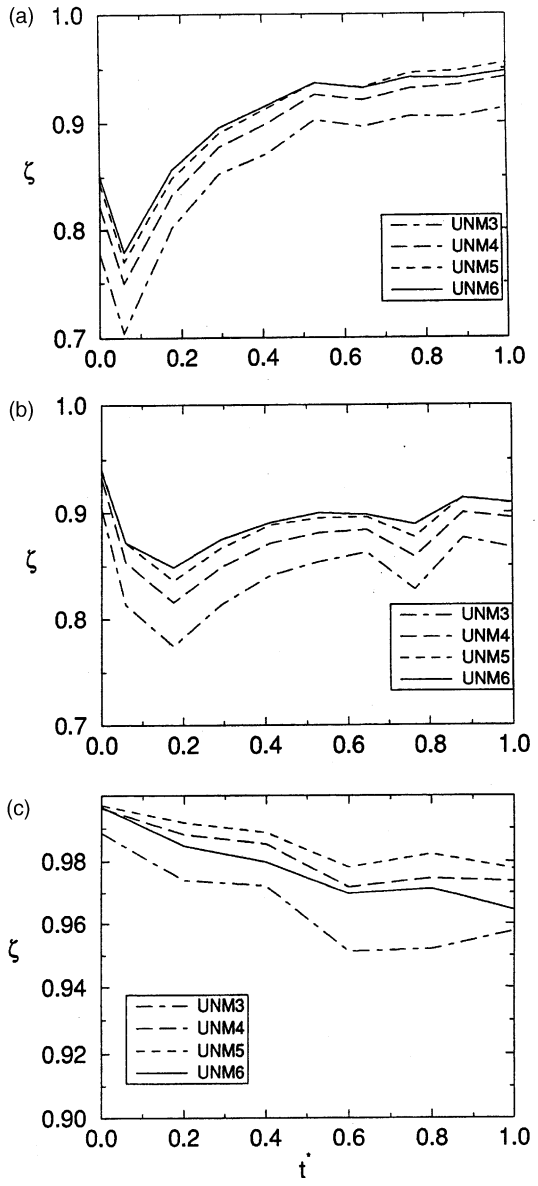

Fig. 4. Temporal variations of the correlation coefficient between the DNS and modeled values of the SGS unmixedness in different flows: (a) HI and $Da = 4$, (b) HS and $Da = 4$, and (c) TSL2 and $Da = 1$.

5. Results of a posteriori analysis

In this section, the subgrid models are assessed a posteriori by conducting LES of various nonreacting and reacting turbulent flows. In nonreacting simulations, the SGS scalar flux models, SFM2, SFM5, and SFM6 are tested. In reacting simulations, the SGS unmixedness models, UNM2, UNM5, and UNM6 are tested. The LES results obtained with other closures indicate that SFM1 is less accurate than SFM2, and SFM3 and SFM4 are less accurate than SFM5. Similarly, we have found that LES results with UNM1 and UNM2 are much less accurate than those with UNM3 and UNM4. The last two models generate less accurate results in comparison to those obtained with UNM5. In all reacting simulations, SFM4 is used as SGS scalar flux model. In all simulations (reacting and nonreacting) a

SGS stress model similar to SFM6 is employed [1]. In a priori analysis (Section 4), the SGS unmixedness models are directly evaluated without referring to the SGS scalar flux models. In a posteriori analysis, the scalar flux models have to be tested first.

5.1. Nonreacting flows

Temporal variation of the resolved scalar variance as obtained by LES with different SGS scalar flux models and by LES with no model are compared with that of DNS in Fig. 5. Evidently, the SGS velocity-scalar correlations are important in both HI and HS flows as LES with no SGS scalar flux model significantly overpredicts the filtered scalar variance. These correlations are correctly represented by SFM5 and SFM6 (see Figs. 1 and 2) and with these models LES predications are close to DNS in both HI and HS flows. Several other statistics of the filtered scalar field as obtained by LES and DNS are plotted in Figs. 6 and 7.

Fig. 6(a) shows the temporal variation of the volumetric-averaged values of the resolved scalar dissipations rate, $\epsilon_A = \gamma \frac{\partial \overline{A}}{\partial x_i} \frac{\partial \overline{B}}{\partial x_i}$ in HS flow. Without any SGS scalar flux model, LES overpredicts $\langle \epsilon_A \rangle$ due to accumulation of the filtered scalar spectra at high wavenumbers. LES with SFM2 also overpredicts $\langle \epsilon_A \rangle$. In fact

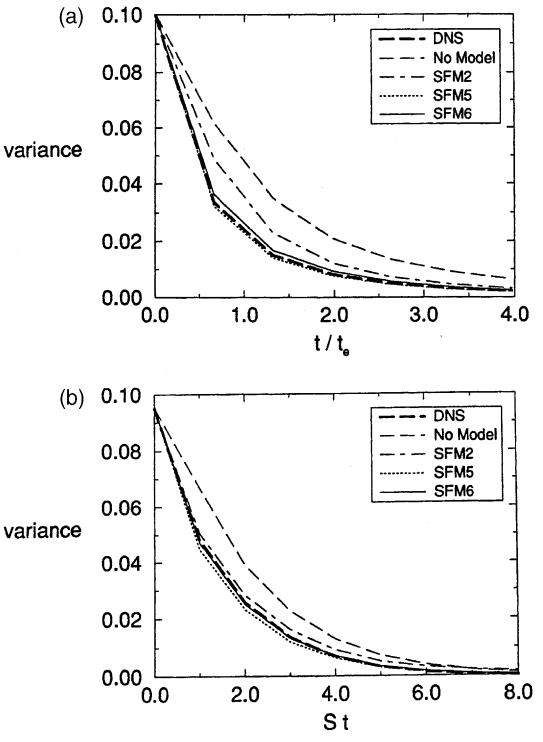

Fig. 5. Temporal variations of the variance of the resolved field scalar $\mathscr{A}$ in different flows: (a) HI and (b) HS.

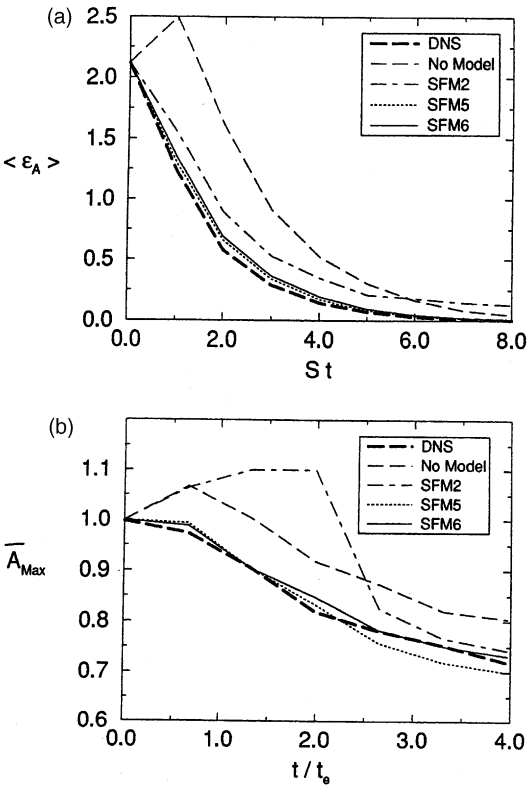

Fig. 6. Temporal variations of (a) the dissipation rate and (b) the maximum concentration, of the resolved field scalar $\mathscr{A}$ in HS flow.

the long time values of $\langle \epsilon_A \rangle$ predicted by SFM2 exceed those of LES with no SGS scalar flux model. This explains the slower decay rate of the scalar variance in Fig. 5 for LES with SFM2. The results obtained via SFM5 and SFM6 are close to DNS results at all times as expected.

Fig. 6(b) shows the temporal variation of the maximum values of the filtered scalar within the computational domain ($\overline{A}_{\max}$) in DNS and LES. In DNS, $\overline{A}_{\max}$ never exceeds unity and properly decays with the decay of the scalar variance. However, in LES, the scalar concentration at some region of the flow may exceeds its maximum allowable (unity) value if a proper subgrid model is not employed. Fig. 6(b) indicates that in the absence of any subgrid scalar flux closure, the magnitude of $\overline{A}_{\max}$ exceeds unity and remains higher than DNS values throughout the simulation. Similar behavior is observed when SFM2 model is used. However, with SFM5 and SFM6 closures LES predicts the evolution of $\overline{A}_{\max}$ with good accuracy.

Fig. 7 shows the PDF of $\overline{A}$, the 3D spectral density function of $\overline{A}(E_A(k))$, and the PDF of τ_{1A} for HI flow at different times. Consistent with the results in Fig. 6, LES with SFM5 and SFM6 predict all these quantities with

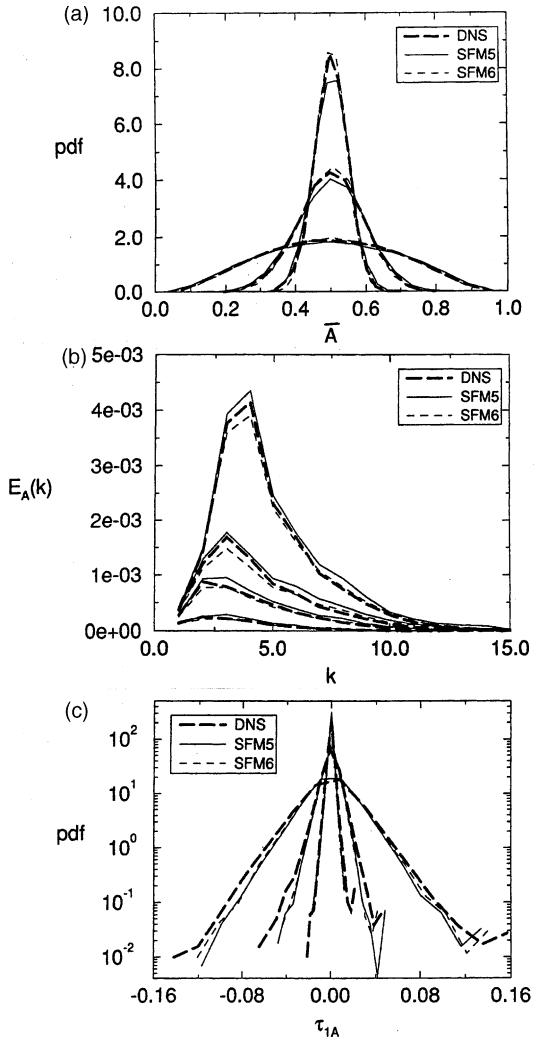

Fig. 7. The statistics of the scalar field in HI flow, (a) the PDFs of the resolved scalar $\mathscr{A}$, (b) the 3D spectral density of the resolved scalar, (c) the PDFs of SGS scalar flux.

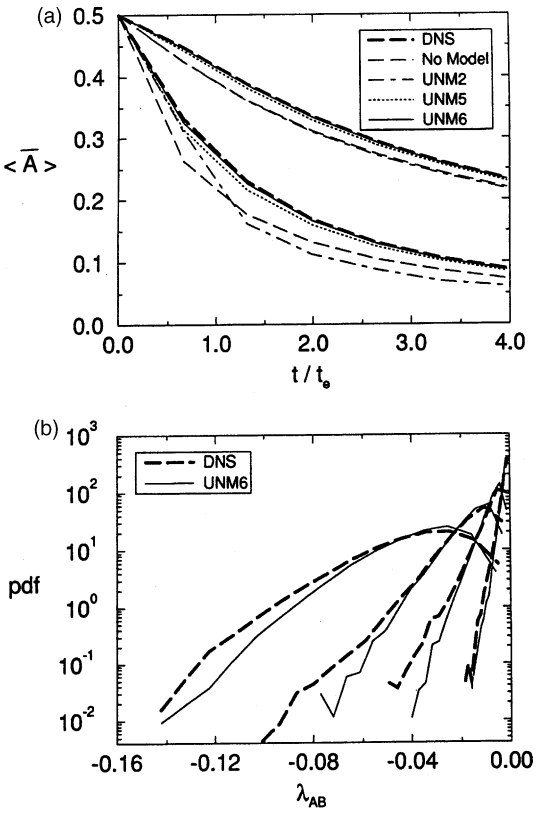

Fig. 8. (a) Temporal variations of the volumetric-averaged values of the resolved field scalar $\mathscr{A}$ in HI flow, (b) the PDFs of the SGS unmixedness in HI flow and for $Da = 4$.

good accuracy. However, without SGS scalar flux model, LES generated results are significantly different than those of DNS; again indicating the importance of subgrid scalar fluctuations. The results for HS and TSL exhibit trends similar to those shown in Fig. 7 for HI flow.

5.2. Reacting flows

In reacting flows, the filtered scalar field is affected by the SGS stress, scalar flux, and unmixedness closures. We have shown that with new serial decomposition models, the SGS stresses and the scalar fluxes and the filtered scalar field are well predicted by LES. Here, we discuss a posteriori performance of the SGS unmixedness in reacting flows.

Fig. 8(a) compares the decay of mean reactant, $\langle \overline{A} \rangle$ as obtained by LES and several different SGS unmixedness closures with that of DNS for different reaction rates in HI flow. Without any unmixedness model, LES underpredicts $\langle \overline{A} \rangle$, more so at higher reaction rates. This is understandable since λ_{AB} has negative effects on the filtered reaction rate (Fig. 3); so if neglected the reaction will appear stronger. The results obtained with UNM2 (or UNM1) do not exhibit any improvement over those with no model. However, LES is able to accurately predict DNS results when UNM5 and UNM6 are employed. This suggests that the serial decomposition closures correctly represent the SGS scalar correlations throughout the simulation. Direct support for this statement is provided in Fig. 8(b), where the PDFs of λ_{AB} as obtained from DNS data are compared with those of LES/UNM6 at different times. It is evident that the DNS and modeled PDFs are very close at all times in this flow.

Figs. 9 and 10 show the temporal variation of $\langle \overline{A} \rangle$, $\langle \overline{AB} \rangle$ and the PDFs of the product mass fraction, $\overline{P}$ in a

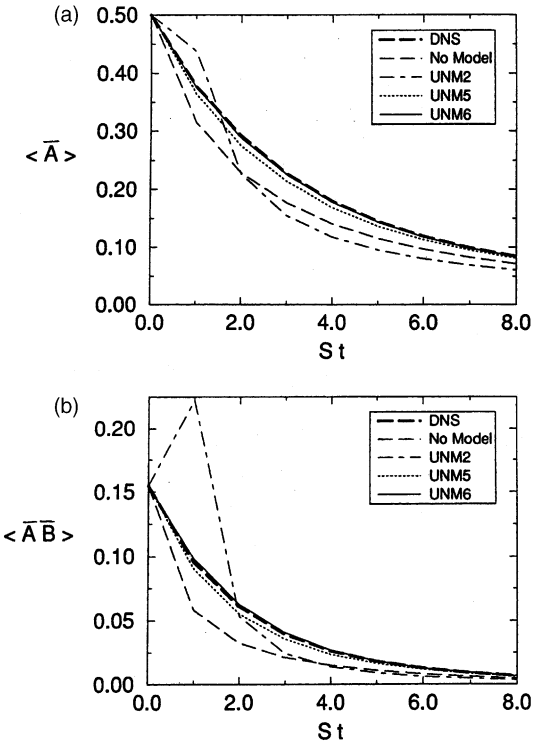

Fig. 9. Temporal variations of different statistics of the resolved field scalars in HS flow for $Da = 4$: (a) $\langle \overline{A} \rangle$ and (b) $\langle \overline{AB} \rangle$.

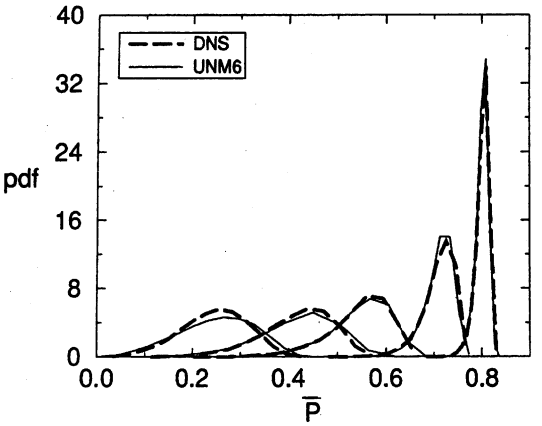

Fig. 10. The PDFs of the resolved field product mass fraction in HS flow and for $Da = 4$.

reacting HS flow. Again, due to importance of subgrid scalar correlations, LES with no unmixedness model (or with UNM2) is unable to correctly predict the decay of $\langle \overline{A} \rangle$ (Fig. 9(a)). The "resolvable" part of the filtered reaction rate (i.e. $\overline{AB}$) is also incorrectly calculated when no SGS model (or UNM2) is used (Fig. 9(b)). However, the predictions improve substantially with incorporation of the serial decomposition models (UNM5 or UNM6). With accurate evaluation of λ_{AB} and $\overline{AB}$, the filtered reaction rate, the reactant conversion rate, and the product formation are correctly predicted by LES at all times. This is demonstrated in Fig. 10, where it is shown that the PDFs of $\overline{P}$ as obtained by LES with UNM6 are very close to those of DNS at all times.

Turbulent mixing layers are often characterized by unsteady large-scale coherent structures [27]. These structures have significant influence on mixing and reaction, and are affected by small (or SGS) scalar correlations. Fig. 11 shows the temporal variation of the product thickness (or the total product mass fraction) as obtained by LES and DNS in TSL1 and TSL2 flows. Consistent with HI and HS flow results, the product thickness is significantly overpredicted by LES when no SGS unmixedness model is used (or when UNM2 is used). However, with the serial decomposition closures (UNM5 or UNM6) LES generates results that are comparable to DNS in both TSL1 and TSL2 flows.

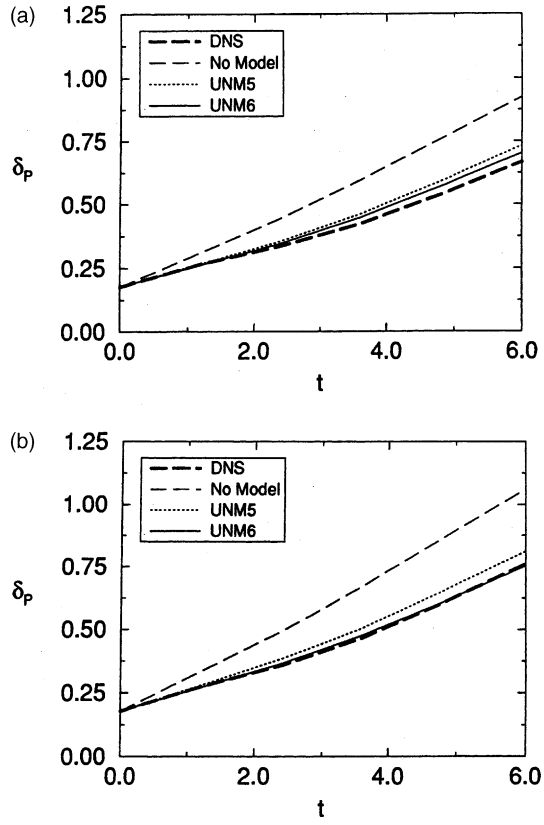

Fig. 11. Temporal variations of the total product mass fraction or product thickness in mixing layer flows and for $Da = 1$: (a) TSL1 and (b) TSL2.

6. Summary and conclusions

LES of scalar (temperature or species concentration) transport in a turbulent flow requires proper closures for the SGS stresses, the SGS scalar fluxes (τ_{iA}), and in case of reacting flow the SGS unmixedness (λ_{AB}). In this paper, we discuss the physical behavior and the modeling of τ_{iA} and λ_{AB}. Four different type of closures are developed/tested: (1) gradient, (2) similarity, (3) mixed similarity-gradient, and (4) serial decomposition closures. All models are assessed (a priori and a posteriori) via analysis of the data gathered from DNS and LES of HI, HS, and temporally developing mixing layer (TSL) flows under nonreacting and nonpremixed reacting flow conditions.

The gradient scalar flux model is developed based on the assumption that the production and the destruction of τ_{iA} are in balance. The similarity and the serial decomposition models are derived based on the observation that the Leonard (L_{iA}), the cross (C_{iA}) and the Reynolds (R_{iA}) parts of τ_{iA} each contribute significantly to the total values of τ_{iA}. Among the tested closures, the serial decomposition models are the most accurate. A priori analysis indicate that both the grid- and test-level SGS scalar fluxes are accurately predicted by these models in all flows and all times. Our a priori results also indicate that the serial decomposition models are the most accurate SGS unmixedness closures regardless of the speed of reaction. Furthermore, we have found that the proposed serial decomposition models are less sensitive to the variations in filter size and/or the approximation in the filtering operation in comparison with other closures.

For a posteriori assessment of the models, LES of HI, HS and TSL flows are conducted in which the models are utilized on localized basis with no averaging over homogeneous directions. In all nonreacting flows, the statistics of the filtered and residual scalar field are accurately predicted by LES when serial decomposition closures are employed. The predictions are much less accurate with gradient or mixed closures. In all reacting flows, the statistics of the resolved scalar field are also correctly represented by LES when serial decomposition unmixedness closures are employed. However, the mean values of the reactants are significantly underpredicted by LES without unmixedness model; indicating the importance of subgrid scalar correlations.

Despite their demonstrated capabilities, the new serial decomposition/similarity models have some limitations in reacting flows. These models (and all the other closures considered in this paper) are developed based on the information residing at large scale or resolved field. In some reacting flows, the small scales have significant dynamic effects on the large-scale variables. For these flows, the models which directly account for the SGS effects (e.g. the FDF model [15,13]) are potentially more accurate.

Acknowledgements

This work is sponsored by the US Office of Naval Research under grant N00014-01-1-0843. Dr. Gabriel Roy is the Program Manager for this grant. Additional Support is provided by National Science Foundation under grant CTS0092665. Acknowledgments is also made to the Donors of the Petroleum Research Funds administered by the American Chemical Society for their support under grant ACS-PRF# 35676-G9. Computational resources are provided by the National Center for Supercomputer Applications (NCSA) at the University of Illinois at Urbana and by the San Diego Supercomputer Center.

References

[1] F.A. Jaberi, P.J. Colucci, Large eddy simulation of heat and mass transport in turbulent flows. Part 1: Velocity field, Int. J. Heat Mass Transfer, in press (doi: 10.1016/S0017-9310(02)00484-2).
[2] M. Ciofalo, Large eddy simulation: a critical survey of models and applications, in: Advances in Heat Transfer, vol. 25, Academic Press, New York, NY, 1994, pp. 321–419.
[3] B. Galperin, S.A. Orszag (Eds.), Large Eddy Simulations of Complex Engineering and Geophysical Flows, Cambridge University Press, Cambridge, UK, 1993.
[4] D. Knight, L. Sakell (Eds.), Fluid Mechanics and its Applications, vol. 54, Kluwer Academic Publishers, The Netherlands, 1999.
[5] T.M. Eidson, Numerical simulation of the turbulent Rayleigh–Benard problem using subgrid modelling, J. Fluid Mech. 158 (1985) 245–268.
[6] P. Moin, W. Squires, W.H. Cabot, S. Lee, A dynamic subgrid-scale model for compressible turbulence and scalar transport, Phys. Fluids A 3 (11) (1991) 2746–2757.
[7] D.K. Lilly, A proposed modification of the germano subgrid-scale closure method, Phys. Fluids A 4 (3) (1992) 633–635.
[8] M.V. Salvetti, S. Banerjee, A priori tests of a new dynamic subgrid-scale model for finite-difference large-eddy simulations, Phys. Fluids 7 (11) (1995) 2831–2847.
[9] U. Schumann, Large eddy simulation of turbulent diffusion with chemical reactions in the convective boundary layer, Atmos. Environ. 23 (8) (1989) 1713–1726.
[10] P. Givi, Model free simulations of turbulent reactive flows, Prog. Energy Combust. Sci. 15 (1989) 1–107.
[11] S.B. Pope, Computations of turbulent combustion: progress and challenges, in: Proceedings of 23rd Symp. (Int.) on Combustion, The Combustion Institute, Pittsburgh, PA, 1990, pp. 591–612.
[12] S. Menon, P.A. McMurtry, A.K. Kerstein, A linear eddy subgrid model of turbulent combustion, in: B. Galperin,

S.A. Orszag (Eds.), Large Eddy Simulations of Complex Engineering and Geophysical Flows, Cambridge University Press, Cambridge, UK, 1993, pp. 287–314 (Chapter 14).

[13] F.A. Jaberi, P.J. Colucci, S. James, P. Givi, S.B. Pope, Filtered mass density function for large eddy simulation of turbulent reacting flows, J. Fluid Mech. 401 (1999) 85–121.

[14] C.K. Madnia, P. Givi, Direct numerical simulation and large eddy simulation of reacting homogeneous turbulence, in: B. Galperin, S.A. Orszag (Eds.), Large Eddy Simulations of Complex Engineering and Geophysical Flows, Cambridge University Press, Cambridge, UK, 1993, pp. 315–346 (Chapter 15).

[15] P.J. Colucci, F.A. Jaberi, P. Givi, S.B. Pope, Filtered density function for large eddy simulation of turbulent reacting flows, Phys. Fluids 10 (2) (1998) 499–515.

[16] A.A. Aldama, Filtering Techniques for Turbulent Flow Simulations, Lecture Notes in Engineering, vol. 49, Springer-Verlag, New York, NY, 1990.

[17] M. Germano, U. Piomelli, P. Moin, W.H. Cabot, A dynamic subgrid-scale eddy viscosity model, Phys. Fluids A 3 (7) (1991) 1760–1765.

[18] F.A. Jaberi, S. James, A dynamic similarity model for large eddy simulation of turbulent combustion, Phys. Fluids 10 (7) (1998) 1775–1777.

[19] P.E. DesJardin, S.H. Frankel, Large eddy simulation of a turbulent nonpremixed reacting jet: application and assessment of subgrid-scale combustion models, Phys. Fluids 10 (9) (1998) 2298–2314.

[20] F.A. Jaberi, R.S. Miller, C.K. Madnia, P. Givi, Non-Gaussian scalar statistics in homogeneous turbulence, J. Fluid Mech. 313 (1996) 241–282.

[21] F.A. Jaberi, Temperature fluctuations in particle-laden homogeneous turbulent flows, Int. J. Heat Mass Transfer 41 (1998) 4081–4093.

[22] F.A. Jaberi, F. Mashayek, Temperature decay in two-phase turbulent flows, Int. J. Heat Mass Transfer 43 (2000) 993–1005.

[23] F.A. Jaberi, D. Livescu, C.K. Madnia, Characteristics of chemically reacting compressible turbulence, Phys. Fluids 12 (5) (2000) 1189–1209.

[24] D. Livescu, F.A. Jaberi, C.K. Madnia, Passive scalar wake behind a Line source in grid turbulence, J. Fluid Mech. 416 (2000) 117–149.

[25] Y. Zang, R.L. Street, J.R. Koseff, A dynamic mixed subgrid-scale model and its application to turbulent recirculating flows, Phys. Fluids A 5 (12) (1993) 3186–3196.

[26] F.M. Najjar, D.K. Tafti, Study of discrete test filters and finite difference approximations for the dynamic subgrid-scale stress model, Phys. Fluids 8 (4) (1996) 1076–1088.

[27] P.E. Dimotakis, Turbulent free shear layer mixing and combustion, in: S.N.B. Murthy, E.T. Curran (Eds.), High Speed Flight Propulsion Systems Progress in Astronautics and Aeronautics, vol. 137, AIAA Publishing Co., Washington, DC, 1991, pp. 265–340 (Chapter 5).